Chemical Science

ROYAL SOCIETY OF CHEMISTRY

EDGE ARTICLE

View Article Online
View Journal | View Issue

Cite this: *Chem. Sci.*, 2025, **16**, 13784

All publication charges for this article have been paid for by the Royal Society of Chemistry

A dual-excitation ratiometric NIR-II fluorescent nanoplatform enables high contrast *in vivo* imaging†

Yongchao Liu, *[ab] Lili Teng,[a] Bo Zhang,[a] Xiao-Bing Zhang [b] and Guosheng Song *[b]

Ratiometric fluorescent probes in the second near-infrared window (NIR-II) with a self-calibration function are sought after for reliable imaging of physiological and pathological processes. Nevertheless, current ratiometric NIR-II fluorescent probes usually show severe spectral overlap in the emission channel, resulting in inevitable sacrifice of the emission intensity of the probe and compromised imaging quality in the NIR-II region. To address these challenges, we developed a novel dual-excitation ratiometric NIR-II fluorescence nanoplatform (DERF-NP), in which the intensity ratio of the same full-wavelength emission from 1000 to 1700 nm under two non-overlapping monochrome excitations with distinct responses is conventionally defined as the quantification parameter. As a proof of concept, DERF-NO, our test case of a ratiometric NIR-II nanoprobe for NO imaging with high sensitivity and quality, was developed based on an energy transfer strategy, which showed increased emission with excitation at 660 nm and constant emission with excitation at 808 nm upon activation of NO. *In vivo* ratiometric NIR-II fluorescence imaging with DERF-NO successfully tracked macrophage polarization and lymphatic metastasis, suggesting the extensive distribution and critical role of macrophages in tumorigenesis and progression. This dual-excitation ratiometric imaging strategy may provide a novel approach for designing ratiometric NIR-II fluorescent probes and has great application potential for intravital imaging analysis.

Received 11th April 2025
Accepted 23rd June 2025

DOI: 10.1039/d5sc02705e

rsc.li/chemical-science

Introduction

Fluorescence imaging in the second near-infrared window (NIR-II, 1000–1700 nm) has attracted increasing attention owing to its high imaging depth, signal-to-background ratio (SBR), and spatial resolution.[1–3] As a result, it can compensate for the deficiency of fluorescence imaging in the first near-infrared window (NIR-I, 700–1000 nm), including tissue absorption, scattering, and interference from the biological background.[4,5] The significantly improved imaging quality makes NIR-II fluorescence imaging a powerful alternative for intravital imaging, such as vascular imaging,[6,7] lymph node imaging,[8,9] tumor surgical navigation,[10,11] disease diagnosis,[12,13] *etc.* As the most promising optical imaging technology, NIR-II fluorescence imaging shows great potential for high-performance imaging research of biological events *in vivo*.[14,15]

Current NIR-II fluorescence imaging probes usually exhibit "off–on" signal conversion based on the single-excitation and single-emission mode, which may be easily affected by the external environment, including the detection conditions, photobleaching, and probe concentration *in vivo*.[16–19] In contrast, ratiometric NIR-II fluorescent probes with a built-in self-calibration function can eliminate or weaken the false signal caused by the external environment, which is conducive to the accurate detection of specific targets in deep tissues compared to the "off–on" probes.[20] As a result, *in vivo* ratiometric NIR-II fluorescence imaging can directly provide reliable visualization information about relevant pathophysiological processes.[21,22] A general strategy for developing ratiometric NIR-II fluorescent probes mainly depends on the imaging mode of single-excitation and double-emission, that is, the ratio of two separate fluorescence emissions in different channels under single-wavelength excitation is defined as a sensitive parameter for quantitative analysis.[23,24] Nevertheless, emission channels usually show severe spectral overlap and crosstalk, and it is an intractable problem to completely separate the two fluorescence emission channels,[25,26] which may result in poor change in the fluorescence ratio and greatly reduce the sensitivity of the

[a]*State Key Laboratory of New Pharmaceutical Preparations and Excipients, Key Laboratory of Medicinal Chemistry and Molecular Diagnosis of Ministry of Education, College of Chemistry and Materials Science, Hebei University, Baoding, 071002, China. E-mail: liuyongchao@hnu.edu.cn*

[b]*State Key Laboratory of Chemo/Biosensing and Chemometrics, College of Chemistry and Chemical Engineering, Hunan University, Changsha, 410082, China. E-mail: songgs@hnu.edu.cn*

† Electronic supplementary information (ESI) available. See DOI: https://doi.org/10.1039/d5sc02705e

probe. Importantly, in order to achieve the ratiometric imaging in two specific channels, multiple filters are usually required to separate the emission channels,[27,28] which inevitably sacrifices the emission intensity of the probe and reduces the imaging quality in the NIR-II window. Consequently, it is urgent to develop novel ratiometric NIR-II fluorescence imaging strategies and probes for high-sensitivity quantitative detection and high-quality intravital imaging, which is of great significance for further promoting the development of NIR-II fluorescence imaging technology in high-performance biosensing and imaging.

In order to overcome the limitations of ratiometric NIR-II fluorescent probes with single-excitation, in this work, we have developed a novel dual-excitation ratiometric NIR-II fluorescence nanoplatform (DERF-NP), in which the intensity ratio (FL_{660ex}/FL_{808ex}) in the NIR-II region under two nonoverlapping monochrome excitations (660 and 808 nm) is conventionally defined as a sensitive parameter for quantitative analysis. Compared with the previously reported ratiometric NO probes that depend on the imaging mode of dual-emission (Table S1†), DERF-NO can effectively overcome the spectral overlap of emission channels and significantly improve the SBR, as it relies on the single-emission imaging mode in the full-wavelength NIR-II region from 1000 to 1700 nm. Additionally, due to the self-calibration of FL_{660ex} and FL_{808ex} in the NIR-II window, this ratiometric imaging strategy of DERF-NP could provide reliable quantitative analysis, and the intensity ratio (FL_{660ex}/FL_{808ex}) is independent of interference factors, including probe concentration, acquisition time, and imaging depth. As a biological proof of concept, DERF-NO, our test case of an NO-responsive NIR-II nanoprobe, was developed based on the dual-excitation ratiometric imaging strategy, which showed increased and constant NIR-II intensity with excitation at 660 nm and 808 nm, respectively, upon the activation of NO. Next, benefiting from the high SBR and resolution *in vivo* imaging, we verified the ability of DERF-NO to specifically detect NO in activated macrophages and metastatic sentinel lymph nodes. We found that the intensity ratio (FL_{660ex}/FL_{808ex}) could, indeed, be used as a noninvasive predictor for real-time evaluation of macrophage polarization in tumor and lymphatic metastasis, indicating that this dual-excitation ratiometric imaging strategy has great application potential for intravital imaging analysis.

Results and discussion

Development of a dual-excitation ratiometric NIR-II fluorescence imaging nanoplatform

Among the many NIR-II organic chromophores, the donor–acceptor–donor (D–A–D)-type chromophores with benzo[1,2-*c*:4,5-*c*′]bis([1,2,5]thiadiazole) (BBTD) as an acceptor unit have been widely applied in intravital NIR-II fluorescence imaging due to their excellent photophysical properties.[29] Furthermore, another selenium analogue (BSBT) was chosen because the replacement of sulfur with selenium usually leads to further band gap reduction and a longer NIR-II emission wavelength (Fig. 1a). Based on this, two NIR-II model chromophores (BBTD and BSBT) were synthesized, and their photophysical properties were investigated. As shown in Fig. S1,† both BBTD and BSBT showed obvious NIR-II emission, and the almost constant fluorescence under irradiation with an 808 nm laser indicated their excellent fluorescence stability compared to ICG. Although the fluorescence quantum yields (QYs) of BBTD and BSBT may not have an advantage compared with many organic molecules or inorganic nanoparticles, they still have great potential in NIR-II fluorescence imaging due to their high photostability and chemical stability.[30] In addition, their extinction coefficient ($\sim 10^4$ M^{-1} cm^{-1}) appeared insufficient by recording their maximum absorbance at 700 and 756 nm, respectively (Table S1†), suggesting their low photon-harvesting capacity, which is not beneficial for NIR-II fluorescence imaging with high brightness. Additionally, owing to their inherent structural inertness, insufficient response sites are available to design activatable NIR-II fluorescent probes for different biological species or physiological processes.

We hypothesized the development of a novel NIR-II fluorescence imaging platform based on BBTD and BSBT chromophores that would (1) improve their photon-harvesting capacity for high-quality intravital imaging and (2) allow for the customization of activatable NIR-II fluorescent probes for quantitative analysis of specific analytes. Currently, Förster resonance energy transfer (FRET) is a flexible probe design strategy because of the diversity of donors and acceptors in the hybrid system,[31,32] which can meet the design requirements for developing ratiometric fluorescent probes. Therefore, we attempted to develop a dual-excitation ratiometric fluorescence nanoplatform (DERF-NP) based on the FRET mechanism using two different fluorophores loaded in a nanoparticle to obtain the ratiometric NIR-II signal. In order to pair up with the absorption of energy acceptors (BBTD or BSBT), three NIR-I chromophores (SIR, BDP and CS) were selected as the representative energy donors because of their molecular designability, high extinction coefficient ($\sim 10^5$ M^{-1} cm^{-1}), quantum yields and excellent photophysical properties[33] (Fig. 1a, Table S2†). The synthetic route is outlined in Scheme S1,† and the new compound structures were confirmed. In the DERF-NP system, energy donors (SIR, BDP and CS) can relay their NIR-I fluorescence to the BBTD or BSBT components to emit NIR-II fluorescence through energy transfer upon excitation at 660 nm, termed FL_{660ex}, and another NIR-II emission (FL_{808ex}) of BBTD or BSBT components served as an internal reference upon excitation at 808 nm. Thus, dual-excitation ratiometric fluorescence imaging can be implemented by self-calibration of the two same full-wavelength NIR-II emissions (FL_{660ex} and FL_{808ex}) from 1000 to 1700 nm upon excitation at 660 nm and 808 nm, respectively (Fig. 1b).

Then, the DERF-NPs were prepared by encapsulation of the model energy donors (SIR, BDP and CS) and acceptors (BBTD and BSBT) with F-127 and PSMA as surfactants (Fig. S2†). As shown in Fig. 1c and d, dynamic light scattering (DLS) revealed similar hydrodynamic diameters of the DERF-NPs, and transmission electron microscopy (TEM) revealed the spherical morphology of these DERF-NPs. And NIR-II fluorescence imaging of DERF-NPs from 1000 to 1700 nm was performed upon excitation at 660 nm and 808 nm, respectively. As shown

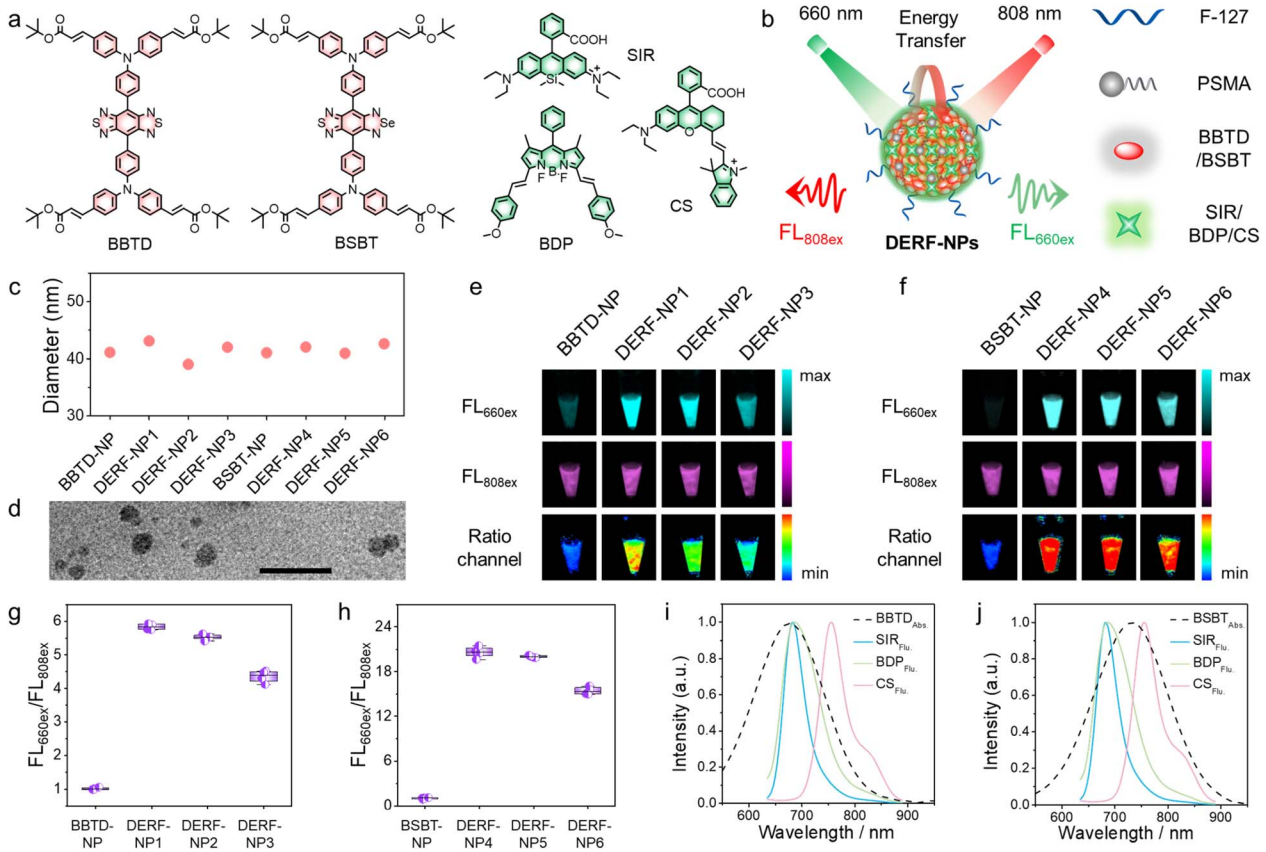

Fig. 1 (a) Chemical structures of energy acceptors (BBTD and BSBT) and donors (SIR, BDP, and CS). (b) Schematic illustration showing the dual-excitation ratiometric NIR-II fluorescence imaging based on the energy transfer mechanism. (c) Representative hydrodynamic diameters of various DERF-NPs measured by DLS (upper panel) and (d) the representative TEM image of DERF-NP4 (bottom panel). Scale bar: 100 nm. (e and f) NIR-II fluorescence images of DERF-NPs with various components. Fluorescence images of DERF-NPs were acquired at 1000–1700 nm upon excitation at 660 nm and 808 nm, respectively. (g and h) Quantification of NIR-II fluorescence intensity ratios (FL_{660ex}/FL_{808ex}) of DERF-NPs in (e) and (f). Spectra overlap shows the absorption spectra of (i) BBTD and (j) BSBT and fluorescence spectra of SIR, BDP, and CS.

in Fig. 1e and f, upon excitation at 660 nm, the NIR-II fluorescence can be barely detectable for the DERF-NPs consisting of only BBTD or BSBT, whereas strong NIR-II fluorescence was observed in SIR-, BDP-, and CS-doped DERF-NPs, indicating that the introduction of NIR-I chromophores into DERF-NPs is beneficial for the enhancement of NIR-II fluorescence intensity. The absorption spectra showed that the absorbance of SIR, BDP and CS was significantly higher than that of BBTD and BSBT at the same molar concentrations (Fig. S3†), which suggests the higher photon-harvesting capacity of SIR, BDP and CS. Importantly, almost constant NIR-II fluorescence of DERF-NPs was observed upon excitation at 808 nm (Fig. 1e and f), which was ascribed to the inherent NIR-II emission of BBTD and BSBT. The obviously decreased NIR-I fluorescence of SIR, BDP, and CS, and increased NIR-II fluorescence of DERF-NPs upon excitation at 660 nm after doping with BBTD or BSBT, collectively indicated the effective energy transfer between the energy donors (SIR, BDP and CS) and acceptors (BBTD and BSBT) (Fig. S4†). In addition, to reveal the influence of tail peaks of SIR, BDP, and CS in the NIR-II region on the fluorescence of DERF-NPs, the NIR-II fluorescence spectra of SIR-NPs, BDP-NPs, CS-NPs, and DERF-NPs under 660/808 nm excitation were measured. As shown in Fig. S5,† the NIR-II fluorescence spectra of these DERF-NPs under 808 nm excitation remain constant due to the exceeded excitation wavelength for SIR, BDP, and CS. In contrast, the fluorescence tail peak of SIR, BDP, and CS under 660 nm excitation does indeed have an impact on the spectra of DERF-NPs, for example, altering their wavelength and shape (especially for DERF-NP3 and DERF-NP6). Fortunately, the fluorescence tail peaks of SIR, BDP, and CS under 660 nm excitation are mainly located in the region from 800 to 1000 nm (Fig. S6†), and their influence on the fluorescence of DERF-NPs in the NIR-II window (1000–1700 nm) is negligible.

The ratiometric fluorescence images and normalized intensity ratio (FL_{660ex}/FL_{808ex}) clearly revealed the fluorescence enhancement of DERF-NPs after doping with SIR, BDP and CS (Fig. 1g and h). It is worth mentioning that DERF-NPs doped with BSBT showed a higher NIR-II fluorescence intensity ratio (FL_{660ex}/FL_{808ex}) compared with BBTD-doped ones, which may be attributed to the low absorbance and fluorescence of BSBT upon excitation at 660 nm. Among these nanoparticles, DERF-NPs consisting of BSBT and SIR (termed DERF-NP4) showed the highest NIR-II fluorescence intensity ratio (FL_{660ex}/FL_{808ex}) compared to the BDP and CS doped ones, which was 21-fold

higher than that of the BSBT-only nanoparticles (Fig. 1h). In order to verify the fluorescence enhancement mechanism of DERF-NPs upon excitation at 660 nm, we compared the extinction coefficients of the donor and acceptor. As shown in Table S1,† the extinction coefficients of SIR, BDP and CS, which are an order of magnitude higher than those of BBTD and BSBT, are sufficient to justify their high photon-harvesting capacity, which results in a significant enhancement of fluorescence of DERF-NPs upon excitation at 660 nm. Additionally, the large spectral overlap between the absorption spectra of energy acceptors and the emission spectra of energy donors can also ensure high efficiency energy transfer in DERF-NPs (Fig. 1i and j). Consequently, based on the energy transfer mechanism, our strategy successfully endowed the resultant DERF-NPs with ratiometric imaging, distinctly broader absorption, great light-harvesting capacity and high NIR-II emission efficiency.

Reliable ratiometric imaging of DERF-NPs both *in vitro* and *in vivo*

Due to the excellent photophysical properties of DERF-NP4, we then applied it for further ratiometric NIR-II fluorescence imaging research in subsequent experiments both *in vitro* and *in vivo*. Generally, the NIR-II fluorescence intensity is dependent on probe concentrations and exposure time. It was assumed that the ratios (FL_{660ex}/FL_{808ex}) of two NIR-II fluorescence intensities upon the excitation at 660 nm and 808 nm would be independent of those interference factors, thereby enhancing reliability for accurate quantification. To confirm this supposition, we systematically investigated the NIR-II fluorescence intensity ratio of DERF-NP4 under different concentrations (Fig. 2a) and exposure time (Fig. 2c) upon excitation at 660 nm and 808 nm, respectively. As expected, the NIR-II fluorescence intensities of both FL_{660ex} and FL_{808ex} were proportional to the probe concentrations (from 2 μg mL^{-1} to 10 μg mL^{-1}) and exposure time (from 20 ms to 100 ms). Surprisingly, the fluorescence intensity ratio (FL_{660ex}/FL_{808ex}) was constant and independent of them (Fig. 2b and d). Furthermore, we explored the luminescence ability of DERF-NP4 in tissues with different thicknesses (Fig. 2e). When intralipid or chicken tissues were placed on top of DERF-NP4, the decreased fluorescence signals (FL_{660ex} and FL_{808ex}) were observed (Fig. 2f and h). Importantly, the fluorescence intensity ratios (FL_{660ex}/FL_{808ex}) were constant with depth of intralipid from 0 to 0.8 cm (Fig. 2g), or chicken tissues from 0 to 0.4 cm (Fig. 2i). Furthermore, we explored the ability of DERF-NP4 for ratiometric imaging of tumor by recording the fluorescence intensities upon excitation at 660 nm and 808 nm at the indicated time points (Fig. 2j). Notably, both the fluorescence intensities upon excitation at 660 nm and 808 nm exhibited a gradual increase from 3 to 24 h, suggesting the accumulation of DERF-NP4 in tumors through the enhanced permeability and retention (EPR) effect. Importantly, the fluorescence intensity ratios (FL_{660ex}/FL_{808ex}) were constant, indicating that they were not affected by the enrichment of concentration and heterogeneous distribution of DERF-NP4 in tumors.

In order to further evaluate the imaging resolution, we have performed lymphatic drainage and angiography in mice as a function of DERF-NP4 administration time. As shown in Fig. S7,† mice were i.d. injected with DERF-NP4 at the rear paw for NIR-II fluorescence imaging. The popliteal and sciatic lymph nodes were clearly identified from all the images acquired post-injection in two emission channels (660 and 808 nm excitation) and their corresponding ratio channel (Fig. 2l). After 10 min post-injection, the afferent and efferent lymphatic vessels connecting the injection site with the two lymph nodes were gradually distinguished. The ratiometric signals of popliteal lymph nodes in DERF-NP4-treated mice showed no obvious change from 10 to 40 min post-injection (Fig. 2m), which demonstrated the ability of DERF-NP4 for reliable imaging of lymph nodes in living mice through ratiometric NIR-II fluorescence imaging. Similarly, carotid and thigh arteries of mice upon excitation at 660 nm and 808 nm can be clearly identified from the acquired fluorescence images by using DERF-NP4 (Fig. 2n), indicating the high-resolution imaging capability of DERF-NP4. The peritoneal blood vessels of mice were also distinguished using filters of different wavelengths, and the filters with longer wavelengths showed weaker brightness and longer exposure time (Fig. S8†), which confirms that the separation of the NIR-II fluorescence emission channel is not beneficial for the acquisition of images with high SBR. It also indicated the inevitability of imaging in the full-band NIR-II region. The above results indicated that dual-excitation ratiometric fluorescence imaging is reliable when imaging the deep-sited tissues, and the main reason for the constant intensity ratios may be attributed to the low background signal of tissues in the NIR-II region.

Activatable dual-excitation ratiometric NIR-II nanoprobe for NO analysis

As a biological proof of concept, our test case of an NO-responsive ratiometric NIR-II fluorescent nanoprobe (DERF-NO) was designed for specific quantification of NO through integrating the NO-responsive molecular probe (SIR-NO), NIR-II chromophore (BSBT), and surfactants (F-127) *via* a self-assembly strategy (Fig. S9a†). The synthetic route of SIR-NO is outlined in Scheme S3.† The fluorescence spectra of SIR-NO after incubation with NO indicated its excellent responsivity to NO, and the spectral overlap of SIR-NO after reaction with NO and BSBT also suggests the efficient energy transfer between them (Fig. S10†). First, we investigated the influence of pH values of buffer solution on the responsivity of DERF-NO toward NO. The absorbance and NIR-II fluorescence of DERF-NO did not change significantly in different pH buffer solutions, indicating that DERF-NO was not sensitive to pH (Fig. S11†). When DERF-NO was incubated with different concentrations of NO in pH 7.0 buffer solution, the absorbance and NIR-II fluorescence showed almost negligible variations, suggesting that DERF-NO cannot detect NO under neutral conditions (Fig. S12†). Afterwards, we attempted to detect NO in acidic buffer solutions, and the results showed that only when the pH of the buffer solution reduced to 5.5 or even 5.0, we can observe the obviously

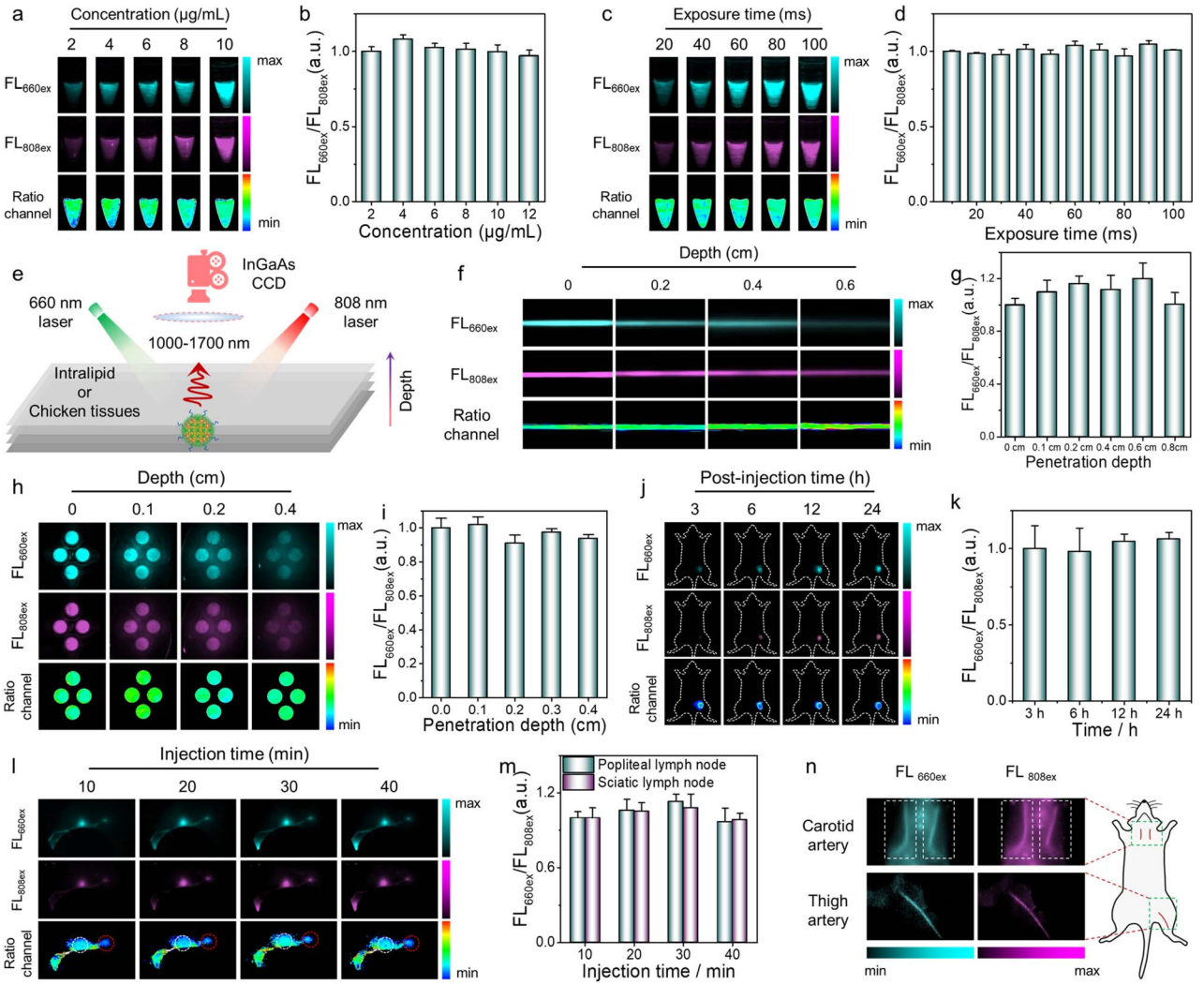

Fig. 2 (a) Representative fluorescence images of DERF-NP4 with different concentrations upon excitation at 660 nm and 808 nm, respectively. (b) Normalized fluorescence intensity ratios (FL_{660ex}/FL_{808ex}) as a function of concentrations of DERF-NP4 in (a). (c) Representative fluorescence images of DERF-NP4 with different exposure time points upon excitation at 660 nm and 808 nm, respectively. (d) Normalized fluorescence intensity ratios (FL_{660ex}/FL_{808ex}) as a function of exposure time of DERF-NP4 in (c). (e) Schematic illustration showing the NIR-II ratiometric fluorescence imaging setup for the tissue phantom study. (f) Fluorescence images of DERF-NP4 through intralipid of different thicknesses. (g) Normalized fluorescence intensity ratios (FL_{660ex}/FL_{808ex}) as a function of thickness of intralipid in (f). (h) Fluorescence images of DERF-NP4 through chicken tissues of different thicknesses. (i) Normalized fluorescence intensity ratios (FL_{660ex}/FL_{808ex}) as a function of thickness of chicken tissues in (h). (j) Representative fluorescence images of mice at different time points after i.v. injection of DERF-NP4. (k) Normalized fluorescence intensity ratios (FL_{660ex}/FL_{808ex}) corresponding to (j). (l) Representative fluorescence images of popliteal (white circle) and sciatic (red circle) lymph nodes after i.d. injection of DERF-NP4 at the rear paw of mice. (m) Normalized fluorescence intensity ratios (FL_{660ex}/FL_{808ex}) obtained from popliteal and sciatic lymph nodes in (l). (n) Representative fluorescence images of carotid and thigh arteries of mice upon excitation at 660 nm and 808 nm, post-i.v. injection of DERF-NP4.

increased absorbance at 660 nm and bright NIR-II fluorescence under 660 nm excitation (Fig. 3c and S13†), which demonstrated that the activation of DERF-NO requires the participation of both NO and acid. In order to reduce the dependence on acid of DERF-NO in NO responsivity, we tried to dope the acidic polymer (polystyrene-*co*-maleic anhydride, PSMA) during the preparation of the nanoprobe (Fig. S9b†), termed DERF-NO (+PSMA). As shown in Fig. 3d and S14,† DERF-NO (+PSMA) showed significantly increased absorbance at 660 nm, and NIR-II fluorescence under 660 nm excitation was observed when the pH value of the buffer solution was reduced to 6.0 or even 6.5. As a comparison, a neutral polymer (polystyrene, PS)-doped DERF-NO was prepared, which still showed the pH-dependent responsivity to NO (Fig. S15†). Given the acidity of PSMA within the nanoprobe DERF-NO (+PSMA), we considered that the introduction of PSMA can greatly relieve the pH-dependent responsivity of SIR-NO toward NO (Fig. 3e). Thus, the PSMA-doped DERF-NO was selected for NO detection in the next experiments. And the DLS and TEM images showed the size and spherical morphology of DERF-NO in diameter (Fig. 3b).

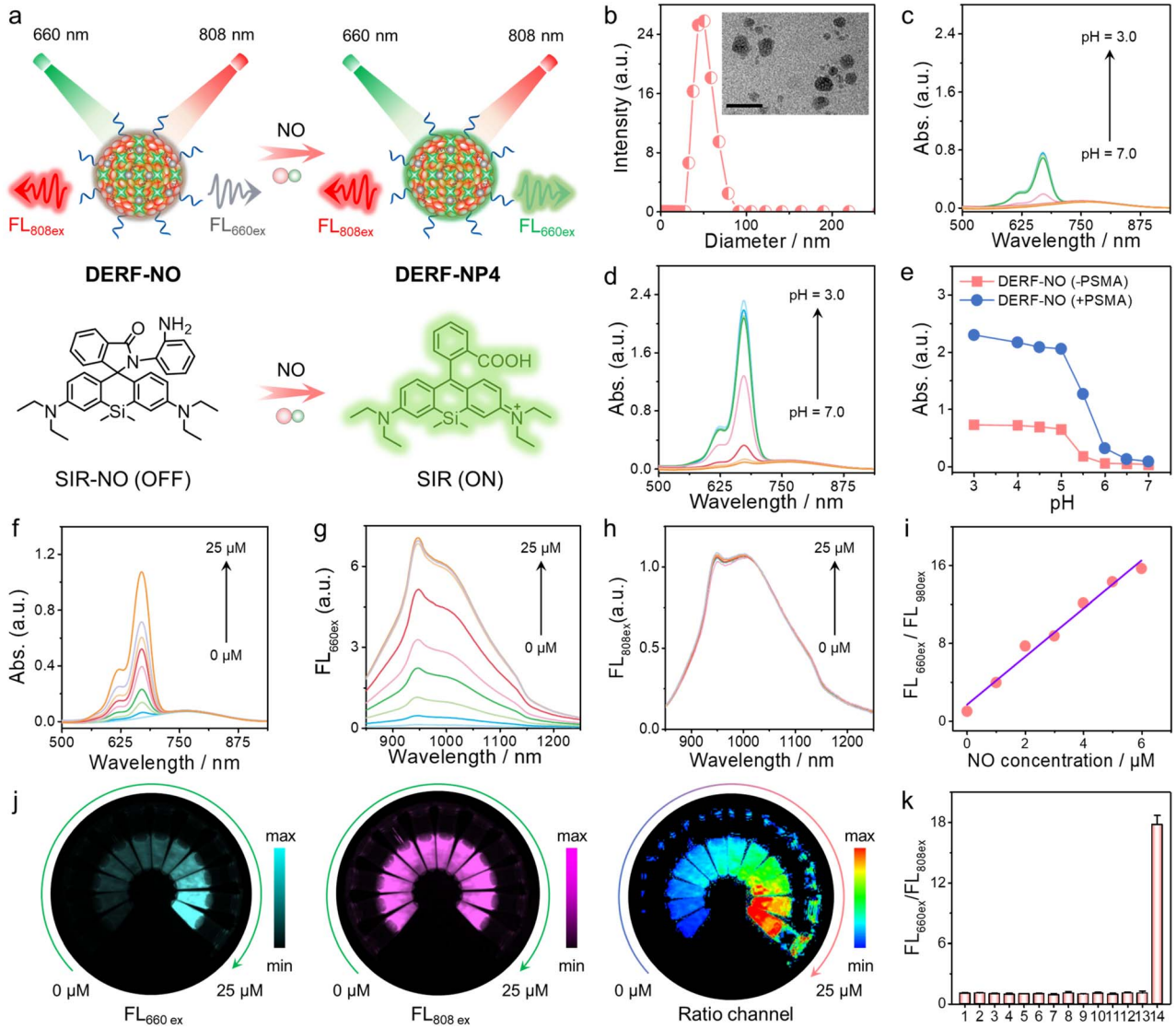

Fig. 3 (a) Schematic illustration showing the ratiometric response of DERF-NO to NO with the dual-excitation ratiometric detection manner, and the chemical structure change of SIR-NO before and after reaction with NO. (b) Dynamic light scattering (DLS) and transmission electron microscopy (TEM) image (inset) of DERF-NO. Scale bar: 100 nm. UV absorption spectra of (c) DERF-NO (−PSMA) and (d) DERF-NO (+PSMA) (10 μg mL^{-1}) treated with NO (25 μM) at different pH values. (e) Quantification of FL_{660ex}/FL_{808ex} of DERF-NO after incubation with NO (25 μM) at different pH values in (c) and (d). (f) UV absorption spectra and fluorescence emission spectra of DERF-NO (10 μg mL^{-1}) treated with different concentrations of NO upon excitation at (g) 660 nm and (h) 808 nm, respectively. (i) Plot of normalized fluorescence intensity ratios (FL_{660ex}/FL_{808ex}) with increasing NO concentration. (j) Representative fluorescence images upon excitation at 660 nm and 808 nm, and corresponding ratiometric images of DERF-NO (10 μg mL^{-1}) treated with different concentrations of NO. (k) Normalized fluorescence intensity ratios (FL_{660ex}/FL_{808ex}) of DERF-NO (10 μg mL^{-1}) upon incubation with different interference species. (1) Blank, (2) Na^+ (10 mM), (3) K^+ (10 mM), (4) Ca^{2+} (10 mM), (5) Fe^{2+} (1 mM), (6) H_2O_2 (250 μM), (7) HClO (50 μM), (8) $ONOO^-$ (50 μM), (9) O_2^- (100 μM), (10) *t*-BuOOH (100 μM), (11) $^{\bullet}OH$ (100 μM), (12) Cys (500 μM), (13) GSH (1 mM), (14) NO (25 μM). Error bars represent the standard deviation of three separate measurements.

After optimizing parameters for the synthesis of DERF-NO, such as surfactants (F127 or DSPE-PEG) and doping amount of BSBT/SIR-NO (from 25% to 200%), the detection ability of PSMA-doped DERF-NO toward NO was then systematically investigated (Fig. S16 and S17†). As expected, with the increased concentrations of NO, the absorbance of DERF-NO gradually increased at 660 nm while remained almost constant at 808 nm (Fig. 3f). Similarly, the fluorescence of DERF-NO at 1028 nm increased significantly upon excitation at 660 nm while remained almost constant upon excitation at 808 nm (Fig. 3g and h). And the quantitative detection of NO could be performed by calculating the fluorescence intensity ratio (FL_{660ex}/FL_{808ex}). As shown in Fig. 3i, the fluorescence intensity ratio (FL_{660ex}/FL_{808ex}) was linearly correlated with NO concentrations from 0 to 6 μM, and the detection limit (3σ/slope) of DERF-NO for NO was calculated to be 45.8 nM, strongly suggesting that this ratiometric strategy of DERF-NO could provide quantitative analysis by self-calibration of the emissions upon excitation at 660 nm and 808 nm, respectively.

The ratiometric NIR-II fluorescence imaging ability of DERF-NO for NO was then investigated. As expected, the NIR-II fluorescence of DERF-NO showed brighter FL_{660ex} and constant FL_{808ex} with the increase of NO concentration upon 660 nm and 808 nm excitation, respectively (Fig. 3j). And the resulting enhanced ratiometric signal of DERF-NO when the concentration of NO was gradually increased also demonstrated that DERF-NO is capable of ratiometric imaging of NO. Additionally, we measured the specificity of DERF-NO and found that only NO could induce the significant enhancement of FL_{660ex}/FL_{808ex} ratios, indicating that DERF-NO was a specific probe for the detection of NO (Fig. 3k and S18†). The selective recognition ability of SIR-NO (the response unit) for NO, and the chemical stability of BSBT (the internal reference unit) in the presence of NO or other interferents collectively result in the specificity of DERF-NO for the detection of NO. In addition, we also investigated the photostability and colloidal stability of DERF-NO. It was clear that fluorescent signals collected at 660 nm and 808 nm of DERF-NO after incubation with NO were comparatively stable (Fig. S19a†), proving that DERF-NO is photostable under physiological conditions. And DERF-NO exhibited good dispersion in PBS, FBS, and DMEM with diameters of ~45 nm during 3 days of measurement (Fig. S19b†), indicating its colloidal stability. These results indicated that DERF-NO was an excellent nanoprobe for ratiometric NIR-II fluorescence imaging of NO with high sensitivity and specificity.

In vivo ratiometric NIR-II fluorescence imaging of macrophage polarization in tumors

Tumor-associated macrophages (TAMs) are a type of immune cell infiltrating the tumor microenvironment, which can exert immunosuppressive properties by polarizing from the M2-phenotype to the anti-tumorigenic M1-phenotype to achieve anticancer efficacy.[34,35] Thus, real-time imaging of macrophage polarization is critical for comprehending the interaction between macrophages and cancer cells, which is of great significance for the evaluation of macrophage function in immunotherapy.[36,37] Owing to the excellent properties of DERF-NO for reliable imaging of NO in solution, we then applied it to evaluate macrophage polarization by real-time ratiometric NIR-II fluorescence imaging of M1-phenotype macrophage-released proinflammatory cytokines (Fig. 4a), such as NO, a hallmark of the polarization of TAMs to the M1-phenotype. Interferon-γ (IFN-γ), a classic macrophage polarization modulator, can stimulate proinflammatory macrophages, induce NO diffusion and inhibit tumor growth.[38] After intratumoral injection of IFN-γ, 4T1 tumor-bearing mice were subsequently i.v.-injected with DERF-NO, and NIR-II fluorescence images of tumors at different post-injection time points were recorded (Fig. 4b). NIR-II fluorescence images showed enhanced fluorescence in both PBS- and IFN-γ treated tumors within 24 h, indicating the accumulation of DERF-NO. Furthermore, IFN-γ-treated tumors maintained consistently strong NIR-II fluorescence upon excitation

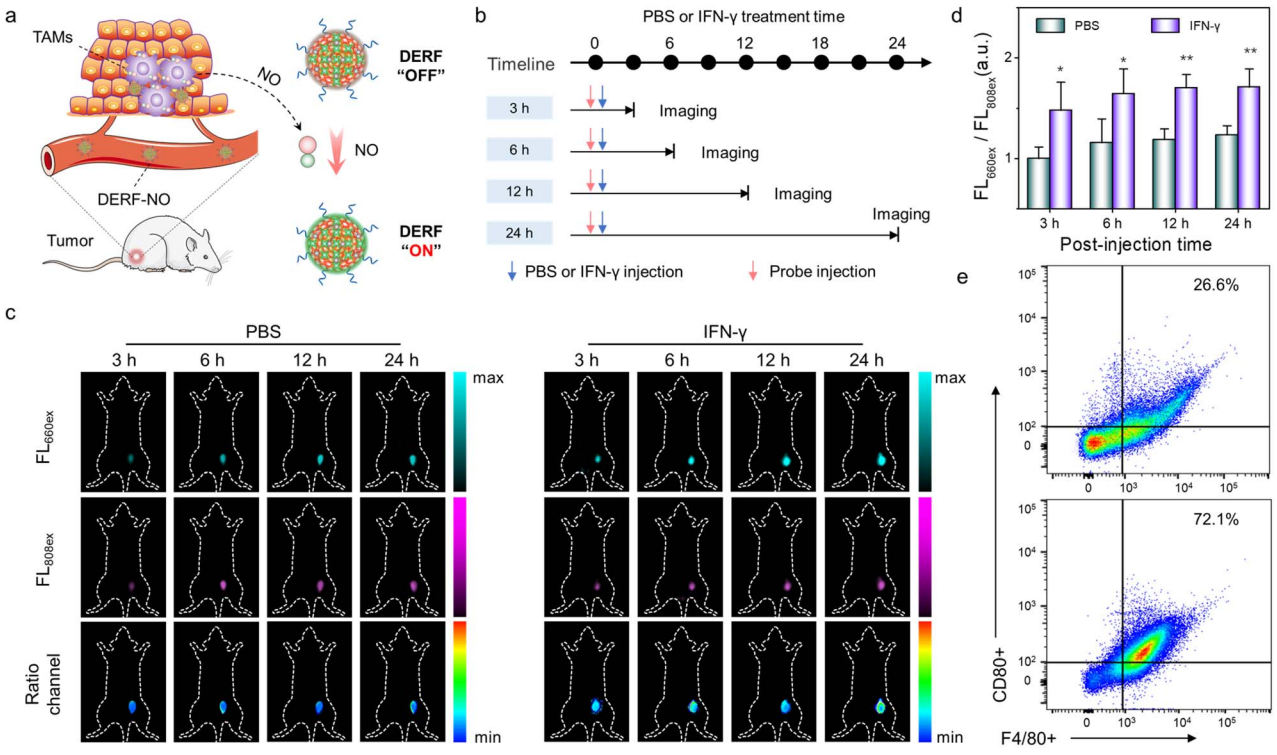

Fig. 4 (a) Schematic illustration showing ratiometric NIR-II fluorescence imaging of NO generation in tumors. (b) The procedure of modulator administration and fluorescence imaging. (c) Representative fluorescence images of 4T1 tumor-bearing mice treated with PBS or IFN-γ (i.t.) and then i.v.-injected with DERF-NO. (d) The corresponding quantification of fluorescence intensity ratios (FL_{660ex}/FL_{808ex}) in (c). (e) Flow cytometric analysis showed the expression of M1-phenotype macrophage marker (CD80) in tumors. $^{**}p < 0.01$, $^{*}p < 0.05$. Error bars represent standard deviation of three separate measurements.

at 660 nm, which may be ascribed to the rapid activation of DERF-NO due to its higher NO concentration in tumors (Fig. 4c). Ratiometric NIR-II fluorescence imaging results showed higher intensity ratios in IFN-γ-treated mice than in control mice, indicating that IFN-γ could induce a higher level of endogenous NO.

Specifically, at 24 h post-injection of IFN-γ, the fluorescence intensity ratios (FL_{660ex}/FL_{808ex}) were 1.23 for the control group and 1.71 for the IFN-γ group, respectively (Fig. 4d). After separating the tumor tissues, *ex vivo* flow cytometric analysis was performed to provide further mechanistic validation of the results obtained using NIR-II fluorescence imaging *in vivo*. As shown in Fig. 4e, all tumors treated with IFN-γ showed higher levels of tumor-associated macrophages with increased M1-phenotype markers (CD80+ F4/80+), corresponding to the higher fluorescence intensity ratio (FL_{660ex}/FL_{808ex}). These results validated the correlation between ratiometric fluorescence intensity and macrophage polarization, demonstrating the potential of DERF-NO as a promising visualization tool for predicting macrophage polarization and screening drugs for macrophage-modulated immunotherapy.

In vivo NIR-II fluorescence imaging of lymph nodes

To further verify the high resolution and sensitivity of DERF-NO for ratiometric NIR-II fluorescence imaging of NO, we then applied it to evaluate the dynamic change of NO in lymph nodes using an animal model of lymphatic inflammation induced by intradermal (i.d.) injection of lipopolysaccharide (LPS). Mice were i.d. injected with LPS or PBS in the rear paw, followed by an additional i.d. injection of DERF-NO after 4 h for NO detection through ratiometric NIR-II fluorescence imaging (Fig. 5a). Significantly, popliteal and sciatic lymph nodes were clearly identified from all NIR-II images upon excitation at 660 and 808 nm and their corresponding ratio images. As shown in Fig. 5b, 30 min post-injection, the afferent and efferent lymphatic vessels connecting the injection site to the two lymph nodes were gradually distinguished. The ratiometric signals of

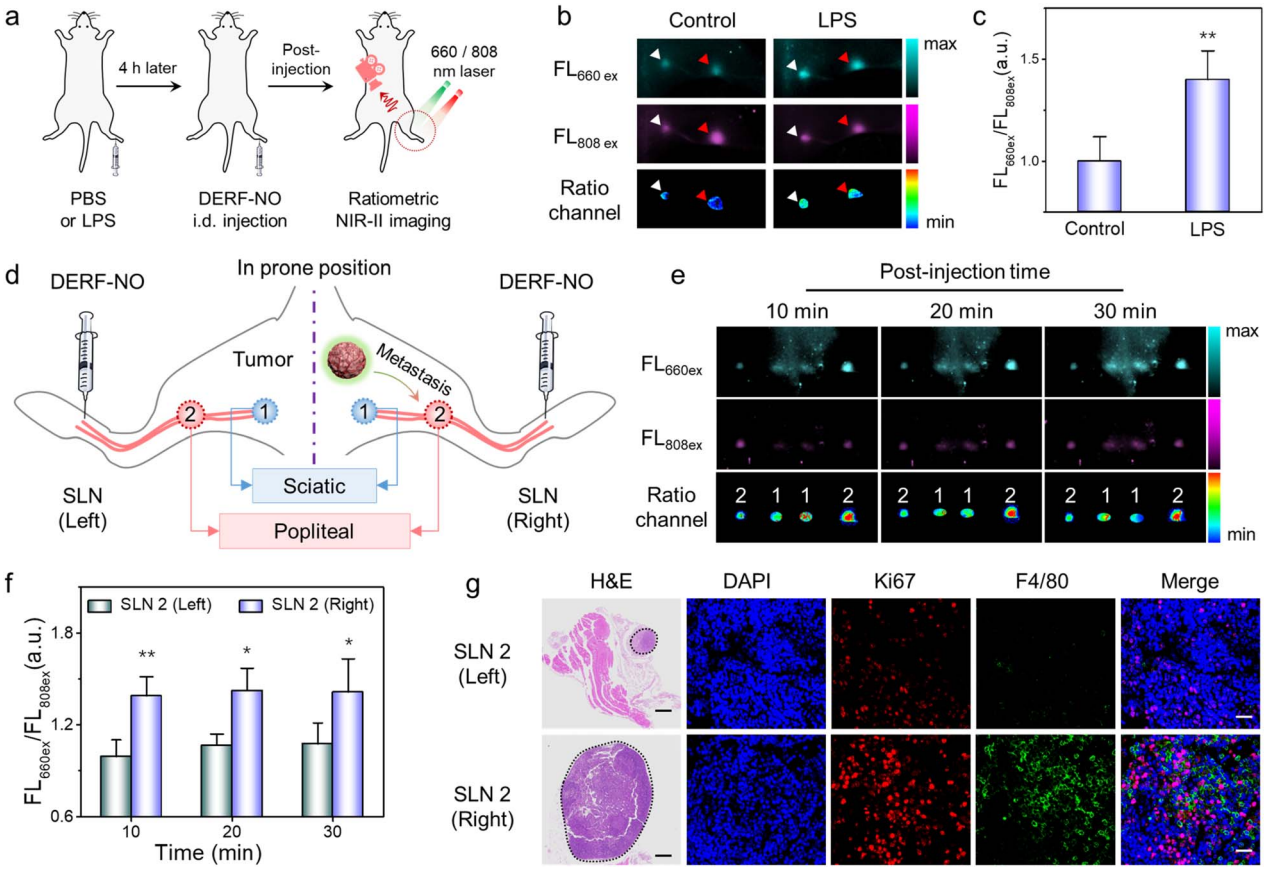

Fig. 5 (a) Schematic illustration showing ratiometric NIR-II fluorescence imaging of LPS-induced lymphatic inflammation using DERF-NO. (b) *In vivo* NIR-II fluorescence images and corresponding ratiometric images of LPS-treated and PBS-treated mice lymphatic drainage post-injection of DERF-NO. The white and red triangles represent sciatic and popliteal lymph nodes, respectively. (c) Ratiometric signals of popliteal lymph nodes obtained from LPS-treated and PBS-treated groups over time. (d) Schematic diagram of *in vivo* NIR-II fluorescence imaging of metastatic tumors in the lymph node. (e) Representative fluorescence images of 4T1-lymph node metastatic mice acquired at different time points. (f) The quantification of corresponding fluorescence intensity ratios of two lymph nodes at different time points in (e). (g) H&E and immunofluorescence staining of excised two lymph node metastatic tumors, in which red represents 4T1 tumor cells (Ki67), green represents macrophages (F4/80), and blue represents cell nuclei (DAPI). $^{**}p < 0.01$, $^{*}p < 0.05$. Error bars represent the standard deviation of three separate measurements.

popliteal lymph nodes in LPS-treated mice increased by approximately 1.39-fold compared to the control group of PBS-treated mice (Fig. 5c). The results demonstrate the ability of DERF-NO to detect NO with high resolution in inflammatory tissues in living mice through ratiometric NIR-II fluorescence imaging.

It has been demonstrated that the phagocytes residing in sentinel lymph nodes (SLNs) can be activated during tumor lymphatic metastasis.[39,40] Nitric oxide activity is highly upregulated during the activation of inflammatory cells such as macrophages, which play an important role in the invasion and metastasis of tumor cells.[41,42] Consequently, real-time monitoring of the level changes of NO in SLNs is key to realizing the visualization of macrophage activity and metastatic imaging of tumor lymph nodes. Furthermore, to visualize and track tumor metastasis in the lymph nodes, we used DERF-NO to investigate macrophage activity in lymphatic metastasis, and *in vivo* NIR-II fluorescence imaging of metastatic tumors in the lymph nodes was performed after intradermal (i.d.) injection of DERF-NO (Fig. 5d). When DERF-NO was injected into the left and right hind paws of 4T1 tumor-bearing mice, obvious NIR-II fluorescence was observed in the popliteal and sciatic lymph nodes of the tumor side (right 1 and 2), whereas the lymph nodes on the normal side (left 1 and 2) of the mice exhibited weak fluorescence (Fig. 5e). In comparison, only weak fluorescence signals were detected in the lymph nodes of the normal sides (left) of mice. The ratiometric fluorescence imaging results and higher intensity ratios were observed in the SLN of the tumor side, indicating that metastatic lymph nodes could generate a higher level of NO. The quantized average intensity ratio (FL_{660ex}/FL_{808ex}) showed that the signal in the area of popliteal lymph nodes on the tumor side was stronger than that on the normal side, indicating that metabolic migration of cancer cells through the lymphatic system indeed occurred (Fig. 5f). H&E staining of the two excised lymph nodes confirmed the existence of metastatic tumors in both of them, and immunofluorescence staining (Ki67 and F4/80) demonstrated an extensive distribution of tumor cells and macrophages in both lymph nodes (Fig. 5g), indicating that the NIR-II fluorescence of the two lymph nodes resulted from metastatic tumors and the polarization of macrophages. Collectively, this study provides preclinical proof of concept for a ratiometric imaging platform to accurately evaluate lymph node status.

Conclusions

In summary, we have developed a novel dual-excitation ratiometric NIR-II fluorescence imaging nanoplatform (DERF-NP) for *in vivo* imaging and molecular sensing. Because the acquired emission channel of DERF-NP covers the full-wavelength range of the NIR-II region, we can achieve ratiometric NIR-II imaging with high quality upon two nonoverlapping monochrome excitations (660 nm and 808 nm), respectively. Such a ratiometric strategy could provide reliable and quantitative analysis by self-calibration of the NIR-II emission under two separate excitations. Theoretically, we can customize various ratiometric imaging probes by introducing responsive units that match the spectrum of the NIR-II fluorophore. For instance, our test case of an activatable nanoprobe (DERF-NO) was developed for NO imaging with high sensitivity and resolution because of the significantly improved SBR and imaging quality in the NIR-II region. This nanoprobe can monitor the fluctuations of NO in macrophage polarization and lymphatic metastasis, which provides a reliable parameter for real-time dynamic evaluation of tumorigenesis and progression. Our work thus opens up a *de novo* ratiometric imaging platform to design various activatable probes for high-performance imaging of biomarkers *in vivo*, which shows great potential in clinical research, including pathogenesis, high-throughput drug screening, *etc.*

Ethical statement

All animal procedures were performed in accordance with the Guidelines for the Care and Use of Laboratory Animals of Hunan University, and the experiments were approved by the Animal Ethics Committee of the College of Biology (Hunan University).

Data availability

All experimental supporting data and procedures are available in the ESI.†

Author contributions

Y. Liu, L. Teng, B. Zhang, G. Song, and X-B. Zhang conceived and designed the experiments; Y. Liu and L. Teng performed the experiments; Y. Liu and G. Song performed data analysis and wrote the manuscript. All authors discussed the results and commented on the manuscript.

Conflicts of interest

There are no conflicts to declare.

Acknowledgements

This work was supported by the National Science Foundation of China (22304043 and 22307032), Natural Science Foundation of Hebei Province (B2023201033), and Science Research Project of Hebei Education Department (BJ2025085 and QN2025171).

Notes and references

1 B. Li, M. Zhao, J. Lin, P. Huang and X. Chen, *Chem. Soc. Rev.*, 2022, **51**, 7692–7714.
2 F. Wang, Y. Zhong, O. Bruns, Y. Liang and H. Dai, *Nat. Photonics*, 2024, **18**, 535–547.
3 J. Mu, M. Xiao, Y. Shi, X. Geng, H. Li, Y. Yin and X. Chen, *Angew. Chem., Int. Ed.*, 2022, **61**, e202114722.
4 Y. Sun, P. Sun, Z. Li, L. Qu and W. Guo, *Chem. Soc. Rev.*, 2022, **51**, 7170–7205.
5 Z. Liu, L. Luo and R. Jin, *Adv. Mater.*, 2023, **36**, 2309073.

6 B. Li, M. Zhao, L. Feng, C. Dou, S. Ding, G. Zhou, L. Lu, H. Zhang, F. Chen, X. Li, G. Li, S. Zhao, C. Jiang, Y. Wang, D. Zhao, Y. Cheng and F. Zhang, *Nat. Commun.*, 2020, **11**, 3012.
7 D. Liu, Z. He, Y. Zhao, Y. Yang, W. Shi, X. Li and H. Ma, *J. Am. Chem. Soc.*, 2021, **143**, 17136–17143.
8 A. Baghdasaryan, F. Wang, F. Ren, Z. Ma, J. Li, X. Zhou, L. Grigoryan, C. Xu and H. Dai, *Nat. Commun.*, 2022, **13**, 5613.
9 R.-X. Wang, Y. Ou, Y. Chen, T.-B. Ren, L. Yuan and X.-B. Zhang, *J. Am. Chem. Soc.*, 2024, **146**, 11669–11678.
10 C. Li, J. Du, G. Jiang, J. Gong, Y. Zhang, M. Yao, J. Wang, L. Wu and B. Z. Tang, *Nat. Commun.*, 2024, **15**, 5832.
11 L. He, Y. Li, C. Zhang, X. Zhang, B. Wang, T. Ren and L. Yuan, *Coord. Chem. Rev.*, 2025, **533**, 216549.
12 J. Chen, L. Chen, Y. Wu, Y. Fang, F. Zeng, S. Wu and Y. Zhao, *Nat. Commun.*, 2021, **12**, 6870.
13 Y. Chen, P. Pei, Z. Lei, X. Zhang, D. Yin and F. Zhang, *Angew. Chem., Int. Ed.*, 2021, **60**, 15809–15815.
14 Z. Lei and F. Zhang, *Angew. Chem., Int. Ed.*, 2021, **60**, 16294–16308.
15 Z. Chen, Y. Zhou, L. Li, W. Ma, Y. Li and Z. Yang, *Small*, 2024, **21**, 2411787.
16 Y. Tang, Y. Li, C. He, Z. Wang, W. Huang, Q. Fan and B. Liu, *Nat. Commun.*, 2025, **16**, 278.
17 Z. Qin, T. B. Ren, H. Zhou, X. Zhang, L. He, Z. Li, X. B. Zhang and L. Yuan, *Angew. Chem., Int. Ed.*, 2022, **61**, e202201541.
18 L. He, L. H. He, S. Xu, T. B. Ren, X. X. Zhang, Z. J. Qin, X. B. Zhang and L. Yuan, *Angew. Chem., Int. Ed.*, 2022, **61**, e202211409.
19 X. Zhang, Y. Chen, H. He, S. Wang, Z. Lei and F. Zhang, *Angew. Chem., Int. Ed.*, 2021, **60**, 26337–26341.
20 M. Zhao, B. Li, H. Zhang and F. Zhang, *Chem. Sci.*, 2021, **12**, 3448–3459.
21 B. Hu, Q. Liu, Y. Jiang, Y. Huang, H. Ji, J. Zhang, X. Wang, X. C. Shen and H. Chen, *Angew. Chem., Int. Ed.*, 2024, **64**, e202418378.
22 F. Chu, B. Feng, Y. Zhou, M. Liu, H. Zhang, M. Liu, Q. Chen, S. Zhang, Y. Ma, J. Dong, F. Chen and W. Zeng, *Chem. Sci.*, 2025, **16**, 4490–4500.
23 Y. Liu, L. Zhang, Y. Chen, H. Sun, J. Chen, A. M. El-Toni, A. Khan, Z. Lei and F. Zhang, *Adv. Opt. Mater.*, 2023, **11**, 2301144.
24 X. Ge, Y. Lou, L. Su, B. Chen, Z. Guo, S. Gao, W. Zhang, T. Chen, J. Song and H. Yang, *Anal. Chem.*, 2020, **92**, 6111–6120.
25 Q. Lan, P. Yu, K. Yan, X. Li, F. Zhang and Z. Lei, *J. Am. Chem. Soc.*, 2022, **144**, 21010–21015.
26 P. Yu, K. Yan, S. Wang, C. Yao, Z. Lei, Y. Tang and F. Zhang, *Nano Lett.*, 2022, **22**, 9732–9740.
27 M. Zhao, J. Wang, Z. Lei, L. Lu, S. Wang, H. Zhang, B. Li and F. Zhang, *Angew. Chem., Int. Ed.*, 2021, **60**, 5091–5095.
28 Z. Lei, C. Sun, P. Pei, S. Wang, D. Li, X. Zhang and F. Zhang, *Angew. Chem., Int. Ed.*, 2019, **58**, 8166–8171.
29 L. Wang, N. Li, W. Wang, A. Mei, J. Shao, W. Wang and X. Dong, *ACS Nano*, 2024, **18**, 4683–4703.
30 Y. Liu, Y. Li, S. Koo, Y. Sun, Y. Liu, X. Liu, Y. Pan, Z. Zhang, M. Du, S. Lu, X. Qiao, J. Gao, X. Wang, Z. Deng, X. Meng, Y. Xiao, J. S. Kim and X. Hong, *Chem. Rev.*, 2021, **122**, 209–268.
31 W. R. Algar, N. Hildebrandt, S. S. Vogel and I. L. Medintz, *Nat. Methods*, 2019, **16**, 815–829.
32 L. Wu, C. Huang, B. P. Emery, A. C. Sedgwick, S. D. Bull, X.-P. He, H. Tian, J. Yoon, J. L. Sessler and T. D. James, *Chem. Soc. Rev.*, 2020, **49**, 5110–5139.
33 S. Samanta, K. Lai, F. Wu, Y. Liu, S. Cai, X. Yang, J. Qu and Z. Yang, *Chem. Soc. Rev.*, 2023, **52**, 7197–7261.
34 S.-L. Li, H.-Y. Hou, X. Chu, Y.-Y. Zhu, Y.-J. Zhang, M.-D. Duan, J. Liu and Y. Liu, *ACS Nano*, 2024, **18**, 7769–7795.
35 C. Liang, Y. Zhang, S. Wang, W. Jiao, J. Guo, N. Zhang and X. Liu, *J. Mater. Chem. B*, 2024, **12**, 4809–4823.
36 N. D. Barth, F. J. Van Dalen, U. Karmakar, M. Bertolini, L. Mendive-Tapia, T. Kitamura, M. Verdoes and M. Vendrell, *Angew. Chem., Int. Ed.*, 2022, **61**, e202207508.
37 J. Huang, M. Xu, P. Cheng, J. Yu, J. Wu and K. Pu, *Angew. Chem., Int. Ed.*, 2024, **63**, e202319780.
38 C. W. Shields IV, M. A. Evans, L. L.-W. Wang, N. Baugh, S. Lyer, D. Wu, Z. Zhao, A. Pusuluri, A. Ukidve, D. C. Pan and S. Mitragotri, *Sci. Adv.*, 2020, **6**, eaaz6579.
39 Z. Wang, H. Xia, B. Chen, Y. Wang, Q. Yin, Y. Yan, Y. Yang, M. Tang, J. Liu, R. Zhao, W. Li, Q. Zhang and Y. Wang, *Angew. Chem., Int. Ed.*, 2021, **60**, 14512–14520.
40 S. Jalkanen and M. Salmi, *Nat. Rev. Immunol.*, 2020, **20**, 566–578.
41 P. Yuan, X. Xu, D. Hu, Y. Chen, J. Fan, S. Yao, Y. Piao, Z. Zhou, S. Shao, N. K. H. Slater, Y. Shen and J. Tang, *J. Am. Chem. Soc.*, 2023, **145**, 7941–7951.
42 C. Lu, S. Liao, B. Chen, L. Xu, N. Wu, D. Lu, H. Kang, X.-B. Zhang and G. Song, *Nat. Mater.*, 2024, **24**, 133–142.